Triller, T., Bataller, H., Bou-Ali, M.M. et al. Thermodiffusion in Ternary Mixtures of Water/Ethanol/Triethylene Glycol: First Report on the DCMIX3-Experiments Performed on the International Space Station. Microgravity Sci. Technol. 30, 295–308 (2018). https://doi.org/10.1007/s12217-018-9598-5

Microgravity-Science and Technology
https://doi.org/10.1007/s12217-018-9598-5

ORIGINAL ARTICLE

Thermodiffusion in Ternary Mixtures of Water/Ethanol/Triethylene Glycol: First Report on the DCMIX3-Experiments Performed on the International Space Station

T. Triller[1] · H. Bataller[2] · M. M. Bou-Ali[3] · M. Braibanti[4] · F. Croccolo[2] · J. M. Ezquerro[5] · Q. Galand[6] · Jna. Gavaldà[7] · E. Lapeira[3] · A. Laverón-Simavilla[5] · T. Lyubimova[8] · A. Mialdun[6] · J. M. Ortiz de Zárate[9] · J. Rodríguez[5] · X. Ruiz[7] · I. I. Ryzhkov[10] · V. Shevtsova[6] · S. Van Vaerenbergh[6] · W. Köhler[1]

Received: 22 December 2017 / Accepted: 6 February 2018

Abstract

We report on thermodiffusion experiments conducted on the International Space Station ISS during fall 2016. These experiments are part of the DCMIX (Diffusion and thermodiffusion Coefficients Measurements in ternary Mixtures) project, which aims at establishing a reliable data base of non-isothermal transport coefficients for selected ternary liquid mixtures. The third campaign, DCMIX3, focuses on aqueous systems with water/ethanol/triethylene glycol as an example, where sign changes of the Soret coefficient have already been reported for certain binary subsystems. Investigations have been carried out with the SODI (Selectable Optical Diagnostics Instrument) instrument, a Mach-Zehnder interferometer set up inside the Microgravity Science Glovebox in the Destiny Module of the ISS. Concentration changes within the liquids have been monitored in response to an external temperature gradient using phase-stepping interferometry. The complete data set has been made available in spring 2017. Due to additionally available measurement time, it was possible to collect a complete data set at 30 °C and an almost complete data set at 25 °C, which significantly exceeds the originally envisaged measurements at a single temperature only. All samples could be measured successfully. The SODI instrument and the DCMIX experiments have proven reliable and robust, allowing to extract meaningful data even in case of unforeseen laser instabilities. First assessments of the data quality have revealed six out of 31 runs with some problems in image contrast and/or phase step stability that will require more sophisticated algorithms. This publication documents all relevant parameters of the conducted experiments and also events that might have an influence on the final results. The compiled information is intended to serve as a starting point for all following data evaluations.

Keywords Diffusion · Thermodiffusion · Soret effect · Ternary mixtures · Microgravity experiments

✉ W. Köhler
werner.koehler@uni-bayreuth.de

1 Physikalisches Institut, Universität Bayreuth, 95440 Bayreuth, Germany

2 Laboratoire des Fluides Complexes et leurs Réservoirs, UMR-5150, E2S - Univ Pau & Pays Adour, 1 Allée du Parc Montaury, 64600 Anglet, France

3 Mechanical and Industrial Manufacturing Department, MGEP Mondragon Goi Eskola Politeknikoa, 20500 Mondragon, Spain

4 ESA-Estec, Noordwijk, The Netherlands

5 E-USOC. ETSIAE, Universidad Politécnica de Madrid, Madrid, Spain

6 MRC, CP165/62, Université libre de Bruxelles, Av. F.D. Roosevelt, 50, 1050 Brussels, Belgium

7 Department of Quṁica Física i Inòrganica, Universitat Rovira i Virgili, Tarragona, Spain

8 Institute of Continuous Media Mechanics UB RAS, 614013 Perm, Russia

9 Departamento de Física Aplicada I, Facultad de Física, Universidad Complutense, 28040 Madrid, Spain

10 Institute of Computational Modelling SB RAS, Federal Research Center KSC SB RAS, Akademgorodok, 660036 Krasnoyarsk, Russia

Preface

This contribution is dedicated to our colleagues and dear friends Jean Claude Legros and Jean Karl Platten, who sadly passed away in 2017. Their fundamental works in the fields of nonequilibrium thermodynamics, fluid mechanics and microgravity research paved the way for modern advances in diffusion and thermodiffusion research and provide a continuous source of inspiration for our efforts.

Introduction

The complexity of diffusion and thermodiffusion processes in multicomponent liquid mixtures grows rapidly with the number of components. While binary mixtures are readily described by two independent coefficients, a Fickian and a thermodiffusion coefficient, ternary mixtures already require six: the four members D_{ij} of the 2×2 diffusion matrix and two thermodiffusion coefficients $D'_{T,i}$, where $i, j = 1, 2$ index the two independent components. Since the total flux must vanish due to mass conservation, the two independent flux densities of a ternary mixtures are

$$\vec{J}_1 = -\rho D'_{T,1} \nabla T - \rho D_{11} \nabla c_1 - \rho D_{12} \nabla c_2 \quad (1)$$

$$\vec{J}_2 = -\rho D'_{T,2} \nabla T - \rho D_{21} \nabla c_1 - \rho D_{22} \nabla c_2 \quad (2)$$

with ρ being the fluid density and c_i the weight fraction of component i (Gebhardt and Köhler 2015a). Only in the binary case are the diffusion and thermodiffusion coefficients independent of the frame of reference (Taylor and Krishna 1993).

Most systems of practical relevance, be it crude oil reservoirs (Galliero et al. 2016) or biological systems, are truly multicomponent and typically contain a larger number of constituents. Because of the many degrees of freedom, a quantitative treatment of such systems with, say, ten components appears hopeless. In this context, ternary mixtures play an important role as model systems. They are still manageable but already show many features characteristic for truly multicomponent systems, such as reverse, osmotic, and cross diffusion.

Because of the associated experimental difficulties, most research on thermodiffusion has been concerned with binary mixtures with water/ethanol as a classical example (Kolodner et al. 1988; Königer et al. 2009; Lapeira et al. 2016). Except for some early experiments (Leaist and Lu 1990; Leahy-Dios et al. 2005; Haugen and Firoozabadi 2005), extensive thermodiffusion measurements on ternary mixtures have started only recently, with the DCMIX (Diffusion and thermodiffusion Coefficients Measurements in ternary Mixtures) project acting as nucleus for most of today's research activities.

The DCMIX project is an international cooperation of several research groups with ESA and ROSCOSMOS to conduct thermodiffusion experiments with ternary liquids in the microgravity environment aboard the ISS. It is the first comprehensive effort to establish a set of reference data guaranteed to be free of gravitational perturbations. Such gravitational instabilities in multicomponent mixtures with temperature gradients can be both of thermal and compositional origin and may perturb on long time scales even an initially stable stratified fluid in thermodiffusion experiments (Lyubimova and Zubova 2014). Due to the additional possibility of cross diffusion, ternary mixture are less predictable and even more prone to this kind of perturbations than binaries. The first diffusion experiment on orbit was IVIDIL (Influence VIbration on DIffusion in Liquids), which focussed on a binary solution. There, the reliability of diffusion coefficient measurements on the ISS inside SODI (Selectable Optical Diagnostics Instrument) could be confirmed (Mazzoni et al. 2010; Shevtsova et al. 2015).

DCMIX is organized into four measurement campaigns, each focusing on particular ternary systems. The aim of DCMIX1, carried out in 2012, was the establishment of a firm basis for ternary mixtures of the hydrocarbons dodecane, isobutylbenzene, and 1,2,3,4-tetrahydronaphthalene. The binary mixtures composed of these compounds are the most-thoroughly studied binary thermodiffusion reference mixtures and have become known as the so-called Fontainebleau benchmark systems (Platten et al. 2003; Gebhardt et al. 2013; Gebhardt and Köhler 2015b, c; Blanco et al. 2010; Sechenyh et al. 2013, 2016; Bou-Ali et al. 2015; Khlybov et al. 2015; Larrañaga et al. 2015; Mialdun et al. 2015; Galand and Van Vaerenbergh 2015; Ahadi and Ziad Saghir 2015). The DCMIX1 mixtures are sometimes regarded as a model for crude oil, containing linear and ring aliphatics as well as aromatic hydrocarbons.

Two years later, in 2014, DCMIX2 comprised five ternary mixtures of toluene, methanol, and cyclohexane, which is a ternary mixture that shows a miscibility gap and a critical point in a certain region of the composition space (Shevtsova et al. 2014a, b; Sechenyh et al. 2012; Lapeira et al. 2017). This system is of particular interest, since it is known from binary mixtures that the Soret coefficient diverges on approach of a consolute critical point (Giglio and Vendramini 1975; Enge and Köhler 2004).

DCMIX3, the mission discussed in this contribution, was flown in 2016 and is coordinated by the team from Bayreuth (in the following called PI-team). In this mission, aqueous mixtures of water (H_2O), ethanol (EtOH), and triethylene

Table 1 Sample compositions of DCMIX3

Cell	c_{H_2O}	c_{EtOH}	c_{TEG}
1	0.20	0.20	0.60
2	0.33	0.33	0.33
3	0.25	0.60	0.15
4	0.75	0.15	0.10
5	0.50	0.10	0.40
6	0.85	0.15	0

All concentrations are given in mass fractions. Cell 6 is the companion cell with the binary mixture

glycol (TEG) have been measured (Shevtsova et al. 2011; Sechenyh et al. 2011; Legros et al. 2015). The sample compositions are listed in Table 1. The DCMIX3-mixtures represent the first aqueous system, and sign changes of the Soret coefficient are to be expected and have already been reported for the binary subsystem water/ethanol (Kolodner et al. 1988; Königer et al. 2009). The optical contrast factors have been determined by the group from Brussels (Shevtsova et al. 2011; Sechenyh et al. 2011).

The presumably last campaign, DCMIX4, is scheduled for 2018 and is presently in preparation. The samples are three additional DCMIX2-mixtures, a nanofluid and a polymer in a mixed solvent.

Originally scheduled for 2014, DCMIX3 was set back by the explosion of the unmanned transport vehicle Cygnus CRS Orb-3 only a few seconds after lift-off, resulting in a complete loss of the DCMIX3 samples aboard the capsule. After the fabrication of a new cell array, the samples arrived at the ISS in July 2016 with SpaceX CRS-9 and the measurements were successfully completed on the 17th of November 2016. Only a small subset of the data was downlinked in real time in order to judge the quality of the measurements. The full data set was stored on flash disks that were brought down to Earth aboard SpaceX CRS-10 and is now available to the science team. The DCMIX3 cell array was destroyed in the atmosphere in the disposal flight of the Cygnus CRS OA-7 in June 2017.

In the following, we will focus on the documentation and preliminary assessment of the raw data gathered during the campaign, quality criteria applied to the data, and the application of evaluation methods first designed for ground-based Optical Beam Deflection (OBD) experiments. "Experiment" contains the details of the DCMIX experiment and the raw data sets, including image processing and phase reconstruction, and lists all carried out measurements. "Assessment of Data Quality" then defines the relevant quality criteria and gives an overview of the quality of the full data set.

Experiment

Selectable Optical Diagnostics Instrument

The DCMIX experiments rely on optical probing of refractive index changes in order to infer time resolved spatial composition changes. Since ternary mixtures are described by two independent composition variables, this involves the use of two different readout wavelengths together with sufficiently different refractive index dispersions of the constituents.

All DCMIX experiments utilize SODI, which is a two-color Mach-Zehnder interferometer equipped with two lasers operating at 670 nm and 935 nm (designated MR and MN for Moving Red and Moving Near-infrared) and a modular cell array with the samples (see Fig. 1). The latter contains five ternary samples and one binary control sample in the so-called companion cell. This companion cell can be measured simultaneously with and independent from the ternary samples utilizing another laser of 670 nm wavelength (designated FR for Fixed Red) in order to detect possible perturbations that could affect the measurements.

SODI is not permanently installed but rather assembled on demand inside the Microgravity Science Glovebox (MSG). The MSG provides power, thermal and control interfaces and an additional containment level, which is of particular importance for experiments using volatile fluids aboard the ISS. SODI comprises the following main components (see Fig. 1):

1. a fixed optical module, housing the FR laser with interferometric optics and CCD camera
2. a movable optical module, housing the MR/MN lasers with interferometric optics and CCD camera
3. the cell array containing five ternary cells and one binary companion cell
4. the SODI main controller and electronics
5. a bottom plate containing the mechanisms and related electronics

The optical modules are designed as Mach-Zehnder interferometers. The laser beams are expanded in order to illuminate the entire sample cell and to record a spatially resolved 2D interference pattern on the CCD camera with a resolution of 1920 × 1080 pixels (Fig. 3 top). The protocol of the thermodiffusion experiments is to prepare an initial equilibrium state and then rapidly switch to a state with a constant temperature gradient across the bulk liquid. This temperature step is followed by much slower mass (thermo)diffusion. Both the temperature and the concentration changes result in refractive index changes, which are converted into phase changes recorded by the interferometer as a time series of interferograms.

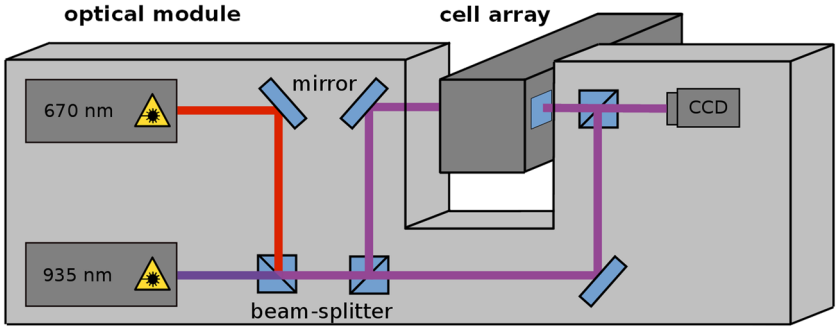

Fig. 1 Schematics of SODI, a Mach-Zehnder type interferometer used for DCMIX measurements. The movable optical module shown here contains the lasers, optical components and a CCD camera and is mounted on a rail. By moving it laterally along the cell array, up to five sample cells with different compositions can be probed. The fixed module, containing only one laser for a binary control sample, is not shown

The cell array and the flash disks to store the data are the only parts that need to be brought to the ISS. The cell array is custom-built for every DCMIX campaign and has to be assembled and filled on ground. The cell design is shown in Fig. 2. Its general layout is similar to Soret diffusion cells used in laboratory experiments. The sample fluid is contained between two parallel copper plates and encompassed by a glass frame. The high thermal conductivity of the copper plates guarantees a uniform heat transfer. On top of the plates, Peltier elements provide the necessary heating/cooling power to establish a constant temperature gradient between the plates. Sensors inside the plates provide temperature data for the regulation of the gradient.

Phase Data Extraction

The interferometric measurements detect a phase change $\Delta\varphi$ of the light of wavelength λ traversing the sample of length L that results from a refractive index change Δn:

$$\Delta\varphi = \frac{2\pi L}{\lambda}\,\Delta n \tag{3}$$

In a two-color experiment, the refractive index change Δn_i at the wavelength λ_i results from the changes Δc_j of the two independent concentrations:

$$\Delta n_i = \sum_{j=1}^{2} \left(\frac{\partial n_i}{\partial c_j}\right)_{T,c_{k\neq j}} \Delta c_j \tag{4}$$

The 2×2 contrast factor matrix $\left(\partial n_i/\partial c_j\right)_{T,c_{k\neq j}}$ needs to be measured separately in laboratory experiments. Phase shifts resulting from the temperature gradient are treated in an analogous way and are neglected for the moment. Their contributions can be separated due to the much faster heat than mass diffusion, corresponding to Lewis numbers $Le = D_{th}/D \sim 10^2$ of liquids (Rapp 2016). Here, D_{th} and D are the thermal and the mass diffusivity.

Phase-stepping interferometry (Robinson and Reid 1993) is used to determine the phase for every pixel in the recorded image. Four consecutive phase steps of $\pi/2$ are implemented by tiny variations of the laser wavelength by means of current tuning, resulting in five consecutive images that are stored in a common image stack (STK) file. The so-called wrapped phase ψ can be evaluated using a modified version (Kreis 2005) of the equation proposed by Hariharan (Hariharan et al. 1987):

$$\psi = \arctan_2\left(\frac{7(I_3 - I_1)}{4I_0 - I_1 - 6I_2 - I_3 + 4I_4}\right) \tag{5}$$

Here, $I_m = I(x, y)_m$ is the two-dimensional intensity information. Due to the four-quadrant inverse tangent function $\arctan_2$ (Robinson and Reid 1993; Ghiglia and Pritt 1998), ψ is still wrapped into the interval $(-\pi, \pi]$ (Fig. 3 middle).

Phase unwrapping is a well-known problem in phase-stepping interferometry, and many different algorithms have been proposed to remove the phase ambiguity (Ghiglia and Pritt 1998). Due to its simplicity, while still producing

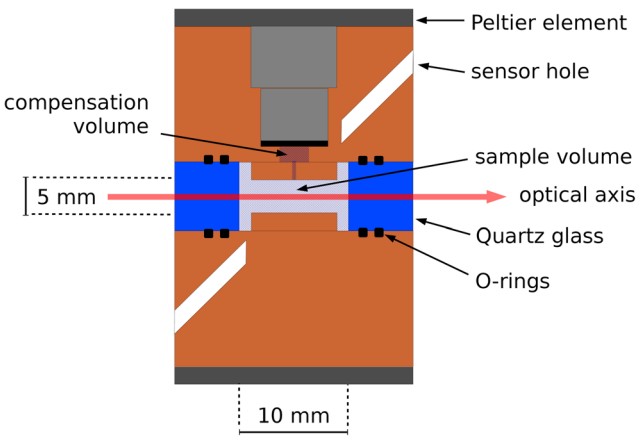

Fig. 2 Schematics of a sample cell. The sample volume of $10 \times 10 \times 5$ mm^3 is sandwiched between two copper plates. Peltier elements on top of the plates are used to establish a temperature gradient

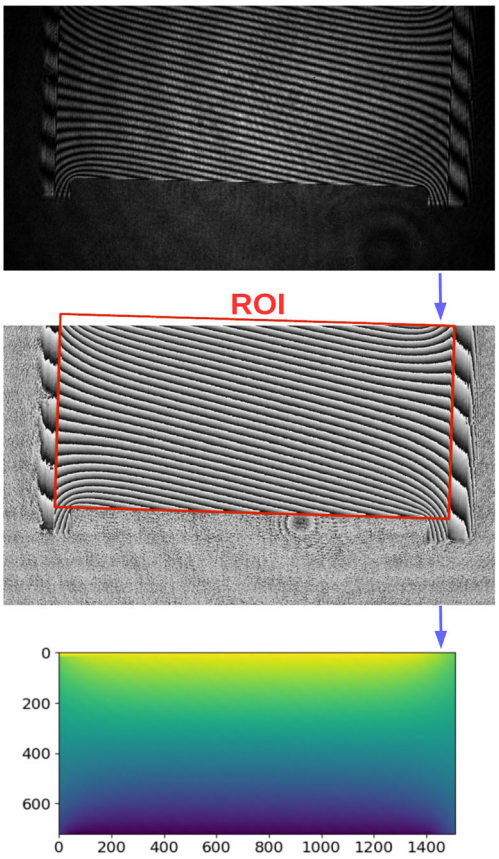

Fig. 3 Top: A two-dimensional interferogram as recorded by the CCD camera for the MR laser. This image is taken from experimental run 01 in cell 1. All images are recorded with a resolution of $N_x \times N_y = 1920 \times 1080$ pixels. Middle: Resulting wrapped phase image from applying Eq. 5 to five consecutive interferograms. Between each interferogram, a artificial phase step of $\pi/2$ is introduced. Bottom: Color-coded image of unwrapped phase $\Delta\varphi(x, y, t)$, after ROI selection and reference image subtraction

acceptable results, we chose a slightly modified version of the algorithm first proposed by Itoh (1982):

$$\varphi(j) = \varphi(0) + \sum_{i=1}^{j} \Phi[\Delta[\Phi[\varphi(i)]]] \quad , \quad j \in [1, N_x] \qquad (6)$$

with

$$\Delta[\varphi(i)] = \varphi(i) - \varphi(i-1)$$
$$\Phi[\varphi(i)] = \psi(i) = \varphi(i) + 2\pi k(i) \quad , \quad k \in \mathbb{Z}$$

Here, j denotes the current pixel along a row of length N_x in the wrapped phase image calculated from Eq. 5. Every row is evaluated independently. This algorithm is rather fast but sensitive to artifacts in the wrapped phase image. To minimize this problem, we select the starting point $\varphi(0)$ not at the image border, which is prone to artifacts, but slice every image into four quadrants, taking the innermost pixels as independent starting points. Typically, the center of the image is free from artifacts and therefore a good starting point for unwrapping.

Before the phase data can be extracted as described above, the images are cropped and rotated in order to exclude regions outside the sample volume and to align the horizontal border of the image to the plates of the cell. This rotation guarantees that the y-axis of the image is parallel to the direction of the temperature gradient (Fig. 3 bottom). After these preparatory steps, the images are of identical rectangular shape, correctly aligned and ready for processing. A reference image is subtracted from every unwrapped phase image, since the individual phase values are only meaningful when compared to an initial state. For all evaluations, we chose the first image in an experimental run as reference image, at a time when the sample is still homogeneous and without temperature gradient.

As shown in Fig. 3, a slight misalignment of the cell array caused a crop of the region of interest (ROI) by five percent in cell 1 and by three percent in cell 2. All other cells are fully covered. Since this slight loss of information is not detrimental for the determination of the transport coefficients, no further action was taken. Any realignment attempt would only have consumed valuable measurement time without a guarantee for success.

Experiment Timeline

All samples were prepared from liquids of high purity: **ethanol** absolute 99.5%, extra dry, AcroSeal® (CAS: 64-17-5) from Acros Organics (lot: 1545382, product code: 397690025); **triethylene glycol** 99% (CAS: 112-27-6) from Acros Organics (lot: A0364772, product code: 139590025); de-ionized and filtrated **water** (resistivity 18.5 MΩcm, 0.22 μm PAK-filter) retrieved from a Millipore Milli-Q® filtration station.

After the complete loss of the samples in 2014 and the fabrication of a new cell array by QinetiQ Space (Belgium), preparations for a new launch (DCMIX3b) started in April 2016 with the mixing of the samples by the PI team. Special care had to be taken to remove any residual gasses from the liquids by a freeze-pump-thaw technique in order to prevent bubble formation inside the cells. After filling of the cell array at the QinetiQ Space facilities, visual inspection of the six cells showed clean samples without any bubbles or other pollutions.

Following experiences from DCMIX2, which suffered from leakages due to insufficient chemical resilience of the sealing material, the DCMIX3b cell array was sealed with Kalrez® O-rings. Extensive compatibility tests had shown significantly less sorption when compared to Chemraz® used during DCMIX2 (Triller et al.).

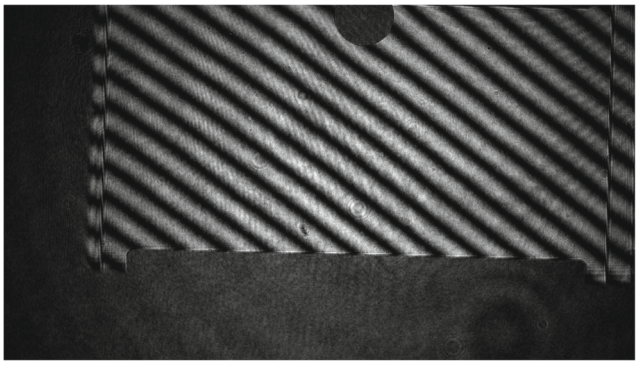

Fig. 4 Cell 3 during checkout operations. A bubble is clearly visible on the top plate near the center of the sample volume

The new DCMIX3b samples were transported to the ISS aboard SpaceX CRS-9 on the 18th of July 2016. With the availability of experiment time for MSG, checkout operations started on the 13th of September. Operations were conducted by NASA astronaut Kathleen Rubins, the crew of the Spanish User Support and Operations Center (E-USOC) in Madrid, engineers of QinetiQ Space, as well as the PI team. A first assessment performed by E-USOC after the assembly of SODI proved that cells 1, 2, 4, 5 and the binary companion cell 6 were in good condition and ready for measurement.

Unfortunately, a bubble had formed inside cell 3 (Fig. 4). It was not immediately clear, whether this bubble resulted from dissolved gasses in the liquid or from leakage. During operations a continuous growth could be observed, indicating some amount of leakage. The estimated bubble volume as measured from the images of cell 3 is plotted in Fig. 5. The volume V grows approximately linearly with time and an extrapolation back to $V = 0$ leads to a date around the end of August for the start of the bubble formation . At this time the cell array had already arrived at the ISS and was waiting for integration into SODI.

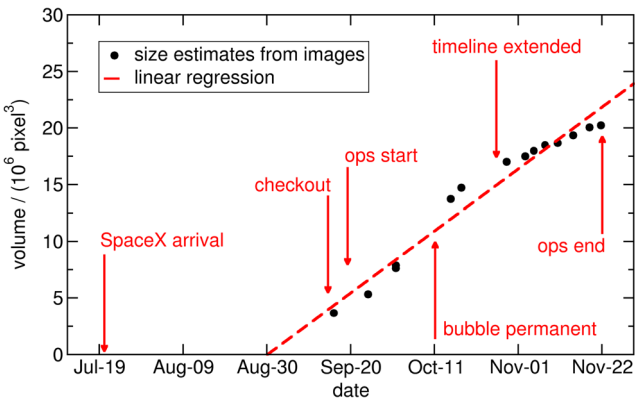

Fig. 5 Volume growth of the bubble in cell 3

To mitigate the impact of the bubble on experiments, several tests were performed in order to trigger some movement or size change. These experiments showed that the bubble could be forced out of the visible cell volume (probably into the compensation volume above the filling hole, see Fig. 2) by heating the cell to 30 °C. Since Marangoni convection at the bubble-liquid interface can easily spoil the results in an unforeseeable way, only one attempt was made to perform measurements for cell 3 at 25 °C in the presence of the bubble. All further measurements for cell 3 were conducted at a mean temperature of 30 °C.

After all mandatory runs had been completed, the time available for the so-called nice-to-have runs was used to measure all other cells also at 30 °C. Hereby, a complete data set for all cells could be obtained for this elevated temperature. The initially considered nice-to-have runs with longer evolution times for the steady state were skipped in favor of the complete data set at 30 °C.

After completion of the setup and the optical checkout, the actual measurements lasted from the 19th of September until the 22nd of November 2016, resulting in a total of 31 experimental runs. Since the generated data amounted to almost half a terabyte, downlinking of the complete data set was not possible. The flash disks with the data had to be removed from the main controller unit and brought back to ground for analysis. A backup of all the science data was copied in an external hard drive that remained on board. The data arrived on the 19th of March via SpaceX CRS-10 and were sent to E-USOC for readout. The integrity of the data was verified, so the on board backup was no longer needed. In June, the complete data set was made available to the science team. All quality assessments presented in "Assessment of Data Quality" refer to the complete data sets.

The mean temperatures and the temperature differences between hot and cold side are summarized in Table 2 for all ternary runs and, if applicable, the simultaneously measured binary companion cell. Due to the need for equilibration, the companion cell could be measured only together with every other ternary run during a continuous measurement period. The timing for all runs was identical to the one defined for the mandatory run in the ESA document *DCMIX3 Experiment Scientific Requirements (ESR)* (Table 3). It comprises a thermalization time of 21 hours at the mean sample temperature T_0 (unmonitored and monitored thermalization), the build-up of the temperature gradient with a high acquisition frequency for 10 minutes followed by three so-called Soret-phases with different acquisition frequencies of 19:50 hours in total. At the end there is a one hour monitored cooling down period. The diffusion phase, during which the equilibrium concentration is restored, has not been recorded due to time constraints.

Table 2 Mean temperature T_0, applied temperature difference ΔT_0 and standard deviations δT for all runs

Run	Cell	T_0 / °C	ΔT_0 / °C	δT_+ / °C	δT_- / °C
5	5	25 (25)	5 (5)	0.0029 (0.0024)	0.0018 (0.0020)
4	4	25	5	0.0222	0.0020
2	2	25	5	0.0033	0.0019
1	1	25 (25)	5 (5)	0.0032 (0.0022)	0.0020 (0.0022)
10	5	25	5	0.0031	0.0018
9	4	25 (25)	5 (5)	0.0223	0.0020
6	1	25	5	0.0031	0.0020
3	3	30 (25)	5 (5)	0.0026 (0.0022)	0.0061 (0.0022)
14	4	25	5	0.0232	0.0020
7	2	25 (25)	5 (5)	0.0031 (0.0022)	0.0019 (0.0021)
15	5	25 (25)	5 (10)	0.0029 (0.0026)	0.0018 (0.0006)
12	2	25	5	0.0031	0.0018
11	1	25 (25)	5 (10)	0.0029 (0.0026)	0.0021 (0.0006)
20	5	25	5	0.0029	0.0019
8	3	30 (25)	5 (5)	0.0025 (0.0022)	0.0062 (0.0020)
16	1	25	5	0.0027	0.0019
13	3	30 (25)	5 (10)	0.0025 (0.0026)	0.0063 (0.0006)
19	4	25 (25)	5 (10)	0.0233 (0.0025)	0.0020 (0.0006)
18	3	30	5	0.0022	0.0021
17	2	25 (25)	5 (10)	0.0025 (0.0024)	0.0019 (0.0006)
20a	5	30	5	0.0030	0.0052
21	4	30 (30)	5 (5)	0.0071 (0.0021)	0.0062 (0.0050)
22	2	30	5	0.0029	0.0044
23	1	30 (30)	5 (5)	0.0025 (0.0025)	0.0058 (0.0049)
24	5	30	5	0.0022	0.0048
25	2	30 (30)	5 (5)	0.0026 (0.0026)	0.0045 (0.0047)
26	4	30	5	0.0072	0.0061
27	5	30 (30)	5 (5)	0.0026 (0.0023)	0.0045 (0.0050)
28	1	30	5	0.0022	0.0054
29	4	30 (30)	5 (5)	0.0071 (0.0022)	0.0063 (0.0050)
30	2	30	5	0.0027	0.0060

$\delta T_{+/-}$ describe the standard deviation of the temperature on the hot/cold plate. The standard deviation is calculated after the gradient has stabilized and describes the mean deviation from the temperature setpoint. Values in parentheses refer to the binary companion cell. Runs in chronological order

Assessment of Data Quality

Image Contrast

As expressed by Eq. 5, phase calculation is performed on a per pixel basis and relies on the intensity variation of the individual pixels during phase stepping. Since the phases of all pixels are shifted simultaneously by, ideally, $\pi/2$ this also results in a shift of the 2D fringe pattern in the direction normal to the fringes. Relevant changes in intensity should only stem from these fringe shifts and not from e.g. variations of the camera sensitivity or the laser intensity between the interferograms. Thus, the contrast stability between the five images of an image stack can serve as a quality criterion.

Some images showed problems in contrast stability during operations as demonstrated in Fig. 6. In order to identify significantly affected runs, we calculate the mean Michelson contrast C_M of an entire run as an average over the Michelson contrasts C_M^i of the individual image stacks $i = 1 \ldots N_s$:

$$C_M = \frac{1}{N_s} \sum_{i=1}^{N_s} C_M^i$$

$$C_M^i = \frac{1}{N_x' N_y'} \sum_{x=1}^{N_x'} \sum_{y=1}^{N_y'} \frac{I_{max}(x,y) - I_{min}(x,y)}{I_{max}(x,y) + I_{min}(x,y)} \quad (7)$$

N_x' and N_y' refer to the 20% × 60% central region of the cropped and rotated images as defined in the ESR. The

Table 3 Timing of the individual runs

Description	Duration [hh:mm:ss]	ΔT	Acquisition frequencies [Hz]
Unmonitored Thermalization	20:00:00	off	-/1
Monitored Thermalization	01:00:00	off	0.01/1
Temp. gradient Build-up	00:10:00	on	0.05/5
Soret 1	00:50:00	on	0.04/1
Soret 2	04:00:00	on	0.01/1
Soret 3	15:00:00	on	0.005/1
Monitored Cooling down	01:00:00	off	0.01/1

The acquisition frequencies are for the images and for the temperatures and TEC (thermo electric cooler, Peltier elements) data. The total on-time of the temperature gradient is 20 hours

coordinates (x, y) identify the individual pixels and N_s is the total number of image stacks within one run. $I_{max}(x, y)$ and $I_{min}(x, y)$ are calculated for every pixel among the five images of every stack. Figure 7 shows the Michelson contrast averaged over all runs. The MR and MN lasers exhibit good contrast in all runs, the contrast of the FR laser drops prominently in runs 08, 13, 19 and 17. The problems resulting for phase calculation in these runs were evident during operations, as many phase images showed distortions not apparent in the RAW images.

Phase Stepping

The drop in contrast discussed above can account for distorted phase information in runs 08, 13, 19 and 17. But in particular phase images acquired with the MR laser also showed distortions, e.g. sudden jumps in the unwrapped phase image, even during runs with good contrast values (see Table 4). Thus, additional factors apart from image contrast are decisive for a successful phase calculation.

In the temporal phase shifting method applied with SODI, a regular phase step of $\pi/2$ is assumed. Variations of the phase steps between individual RAW images directly lead to errors in the calculated phase. As a quantitative measure an estimation of the phase steps is necessary. Again, this problem is well studied in the literature, and different estimation methods have been proposed over the years. Due to its simplicity, we chose the Carre phase estimation algorithm (Servin et al. 2014), which estimates the average phase step ω_0 from four intensity values $I_0 \ldots I_3$:

$$\tan(\omega_0/2) = \sqrt{\frac{3(I_1 - I_2) - I_0 + I_3}{I_0 + I_1 - I_2 - I_3}} \tag{8}$$

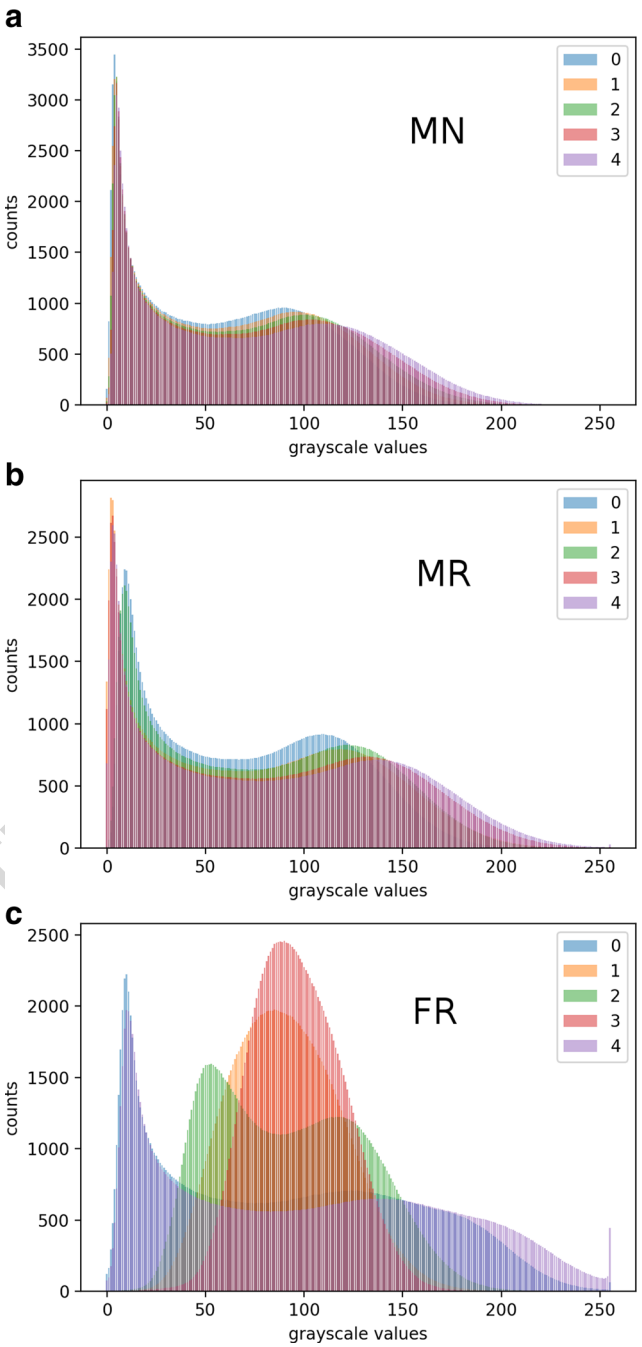

Fig. 6 Histograms from run 17. The MN and MR lasers shows a stable contrast behavior with similar histograms of the five RAW images of a stack. The FR laser shows a strong deviation from the bimodal distribution expected from a sinusoidal interference pattern

Eq. 8 is applied to a single pixel from four consecutive images in an image stack. The phase step ω_0 is then averaged over the entire image plane and over all stacks in a run in the same way as the Michelson contrast in Eq. 7. This algorithm can only estimate the average step, but it cannot make predictions about individual phase steps between images. Nevertheless, the algorithm is sufficient to

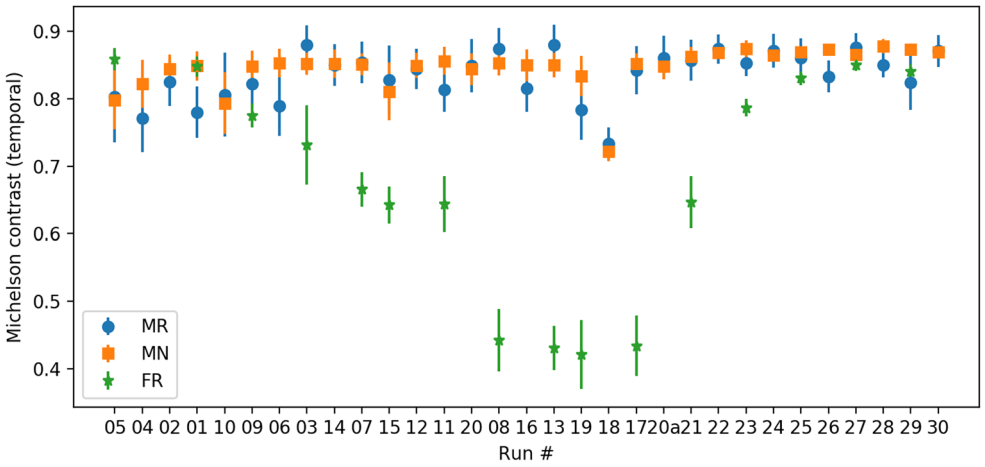

Fig. 7 The averaged Michelson contrast C_M (see Eq. 7) of all experimental runs performed during DCMIX3 operations (runs are sorted in chronological order). Error bars are taken from the averaged standard deviation of all image stacks in one run. The FR laser shows strong deviations of the contrast, with C_M dropping below a critical threshold of 0.5 during runs 08, 13, 19 and 17

Table 4 Michelson contrast C_M and estimated phase step ω_0 for all runs and lasers

		MR			MN			FR		
Run	Cell	C_M	ω_0/π	low SNR	C_M	ω_0/π	low SNR	C_M	ω_0/π	low SNR
5	5	0.80	0.63 / 0.64	*	0.80	0.58 / 0.60	*	0.86	0.54 / 0.52	
4	4	0.77	0.58 / 0.57	*	0.82	0.54 / 0.55				
2	2	0.82	0.53 / 0.54		0.84	0.50 / 0.51				
1	1	0.78	0.53 / 0.55		0.85	0.49 / 0.50		0.85	0.54 / 0.52	
10	5	0.81	0.63 / 0.63	*	0.79	0.58 / 0.59	*			
9	4	0.82	0.52 / 0.52		0.85	0.50 / 0.51		0.77	0.53 / 0.53	
6	1	0.79	0.54 / 0.56		0.85	0.50 / 0.50				
3	3	0.88	0.50 / 0.50		0.85	0.49 / 0.51		0.73	0.51 / 0.54	
14	4	0.85	0.51 / 0.51		0.85	0.50 / 0.51				
7	2	0.85	0.51 / 0.52		0.85	0.49 / 0.50		0.67	0.41 / 0.54	
15	5	0.83	0.59 / 0.59	*	0.81	0.54 / 0.55		0.64	0.44 / 0.50	
12	2	0.84	0.53 / 0.51		0.85	0.49 / 0.51				
11	1	0.81	0.54 / 0.52		0.86	0.49 / 0.50		0.64	0.53 / 0.55	
20	5	0.85	0.56 / 0.54		0.84	0.51 / 0.52				
8	3	0.87	0.49 / 0.51	(bubble)	0.85	0.50 / 0.51	(bubble)	0.44	0.69 / 0.77	*
16	1	0.81	0.62 / 0.52		0.85	0.49 / 0.50				
13	3	0.88	0.50 / 0.51	(bubble)	0.85	0.50 / 0.51	(bubble)	0.43	0.65 / 0.75	*
19	4	0.78	0.54 / 0.56	*	0.83	0.52 / 0.52		0.42	0.64 / 0.64	*
18	3	0.73	0.56 / 0.51	(bubble)	0.72	0.50 / 0.51	(bubble)			
17	2	0.84	0.54 / 0.52		0.85	0.50 / 0.51		0.43	0.66 / 0.67	*
20a	5	0.86	0.54 / 0.53		0.85	0.50 / 0.51				
21	4	0.86	0.55 / 0.50		0.86	0.50 / 0.51		0.65	0.71 / 0.64	*
22	2	0.87	0.56 / 0.51		0.87	0.50 / 0.51				
23	1	0.85	0.68 / 0.51		0.87	0.49 / 0.50		0.79	0.57 / 0.53	
24	5	0.87	0.51 / 0.53		0.86	0.50 / 0.51				
25	2	0.86	0.52 / 0.54		0.87	0.50 / 0.51		0.83	0.51 / 0.52	
26	4	0.83	0.50 / 0.48	*	0.87	0.51 / 0.52				
27	5	0.88	0.51 / 0.51		0.87	0.50 / 0.51		0.85	0.52 / 0.52	
28	1	0.85	0.69 / 0.50		0.88	0.50 / 0.51				
29	4	0.82	0.59 / 0.50		0.87	0.51 / 0.52		0.84	0.51 / 0.52	
30	2	0.87	0.53 / 0.49		0.87	0.50 / 0.51				

The FR laser always probes the binary companion cell 6. Runs in chronological order. The runs with low SNR of the extracted phase images are marked by an asterisk. Runs 8, 13, and 18 are affected by a bubble in cell 3

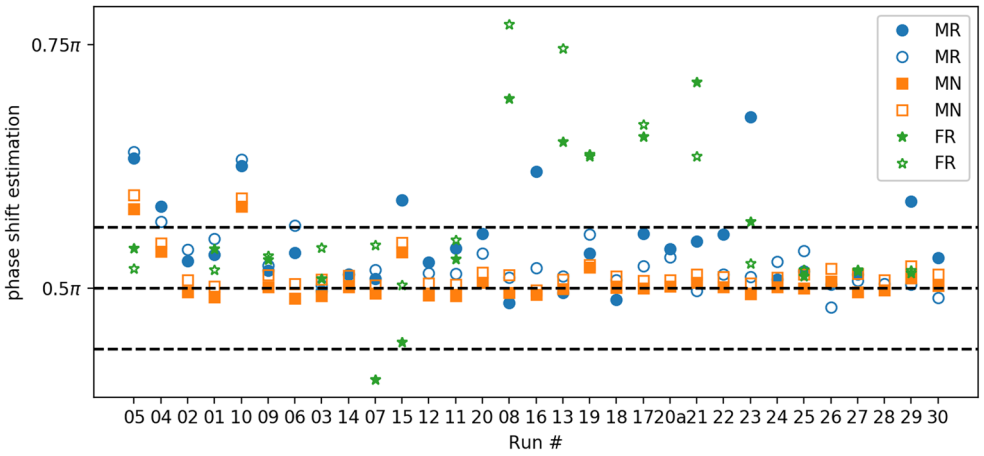

Fig. 8 The estimated phase step of all experimental runs, as calculated according to Eq. 8. Closed symbols represent values calculated from images $I_0 - I_3$, open symbols to values from images $I_1 - I_4$. The dashed lines mark a deviation of $\pm 1/16\pi$ from the desired phase step of 0.5π, which translates to about one percent error in the phase calculation (Servin et al. 2014)

give some indication for overall problematic phase stepping behavior. Since it uses only four images, it can be applied either to images $I_0 - I_3$ or to $I_1 - I_4$ from the SODI image stacks. Results for all runs are visualized in Fig. 8 and summarized in Table 4.

The consequences of poor phase stepping are demonstrated in Fig. 9. It shows a preliminary data evaluation based on the slope of the phase gradient (lower picture in Fig. 3) in the center of the cell. The difference between run 01 (MN) and run 05 (MR) is evident. The latter suffers from severe perturbations, which is also reflected in its apparently too large phase step $\omega_0 = 0.63\,\pi$ as compared to the almost perfect value $\omega_0 = 0.49\,\pi$ for the noise-free run 01 (MN). Luckily, the information contained in the SODI images and phase stacks contains sufficient redundancy and the phase gradient can also be reconstructed from the spatial variations of the fringe patterns without loosing any of the affected runs.

Temperature Control

An important parameter for all thermodiffusion experiments is the temperature control. Since the refractive index $n(T, c_j)$ depends on both the temperature T and the concentrations c_j, one has to rely on the different timescales of heat and mass diffusion to separate these contributions. Ideally, the temperature difference is applied with a Heaviside step function, observing the evolution of the temperature and the concentration fields within the sample on longer time scales. This necessitates a precise temperature control, able to switch a temperature gradient on short timescales, but also to keep this gradient stable on long timescales.

The temperature control is implemented via Peltier elements on the top and bottom of the cell. To maximize the thermal conductivity, while minimizing corrosion due to the long-term exposure to chemicals, the cells are made from nickel-plated copper (see also Fig. 2). Temperature sensors allow to implement a proportional-integral-differential feedback loop for temperature control. The sensors are sampled with 1 Hz (5 Hz during the temperature build-up phase) and the readouts are stored together with the image data. A calibration of this feedback loop was performed after the cell array had been inserted into SODI.

Figure 10 shows the temperature profiles for the hot and the cold plate of cell 4 during run 04. The characteristic switching time constant is on the order of 22 seconds. The temperatures are stable and show no significant deviations, except for Peltier number 9 on cell 4. This Peltier element showed noticeable fluctuations at frequencies between 0.01 and 0.1 Hz during runs 4, 9, 14 and 19. Run 4 is shown as an example in Fig. 10. Since the sample itself acts as a low pass filter, this high frequency noise is sufficiently suppressed and does not negatively affect the final signal. Table 2 gives a summary of the temperature stability by listing the standard deviation of the temperature readings after gradient buildup. Curiously, the noise level for Peltier 9 drops significantly for all runs executed with a mean temperature of $T_0 = 30\,^{\circ}\mathrm{C}$.

Vibrational Characterization

The long duration of the individual runs made an accurate characterization of its accelerometric history particularly valuable in order to assess potential impacts of disturbances on the quality of the experimental results. Nevertheless, this characterization is only complementary, because the presence of disturbances does not necessarily imply their subsequent influence on the data quality. To achieve this purpose, information coming from different sensors located at different places of the same module or even in different modules of the ISS has be used. All sensor data have been downloaded from the PIMS NASA website (https://pims.grc.nasa.gov/). Details of the different events accounted for in all

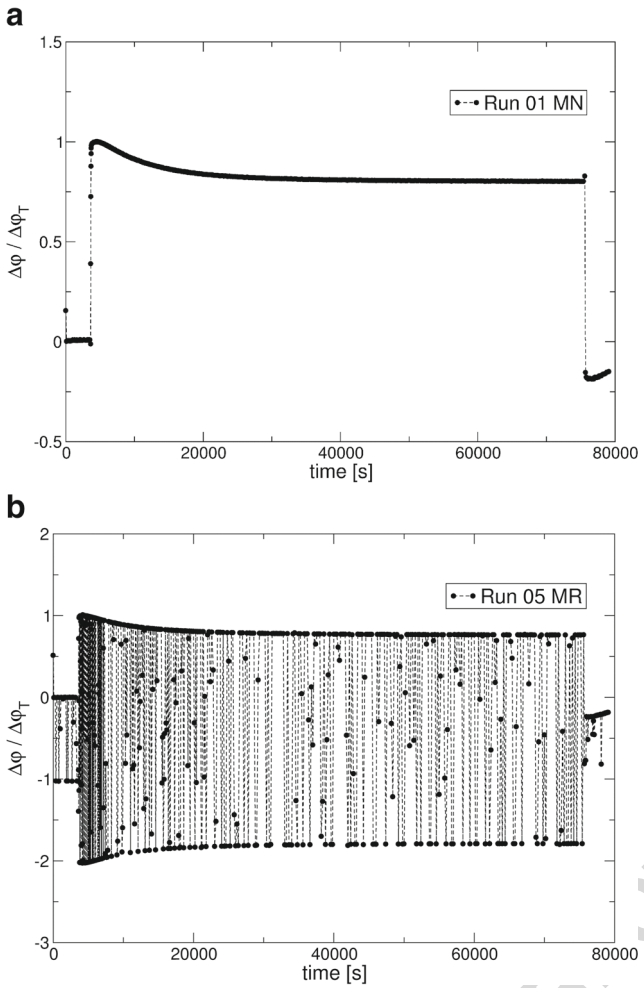

Fig. 9 Preliminary data evaluation showing the phase gradient in the center of the cell after normalization to the amplitude of the purely thermal contribution. Run 05 (MR) shown in the lower sub-figure suffers from significant laser phase stepping instabilities

runs were provided by the Spanish USOC, which remotely operated the experiment (https://www.eusoc.upm.es/).

A detailed analysis of vibrations during DCMIX2 and DCMIX3 has been given in Refs. (Dubert et al. 2017; Ollé et al. 2017) The mathematical characterization of the acceleration signals is based on an accurate minute by minute evolution of the different magnitudes such as, for instance, the root mean square (RMS), the spectral entropy (SEN), and the frequency factor index (FFI). The last two quantities have recently been introduced in the literature as new techniques for the characterization of acceleration signals. The Shannon entropy allows to study the regularity of the power distribution in time for a specific signal and has the same sensitivity against disturbances as the RMS. A particular advantage of using the spectral entropy as a signal disturbance indicator is that the contributions of different frequency bands could be explicitly considered with the aim of observing their specific changes (Dubert et al. 2017; Ollé et al. 2017).

As an example, Fig. 11 presents the RMS and SEN evolution for the three acceleration components of run 23. There is a good correlation between the spikes detected by these two different techniques. The FFI defined in Ref. Ollé et al. (2017) is a scalar indicating a logarithmic relationship between the absolute maximum of the power spectral density (PSD) of the whole frequency range with respect to the relative maximum PSD value for a predefined low frequency range. High values indicate little influence of the above mentioned low frequencies on the ongoing run. Finally the minute by minute RMS contribution over each one of the one-third octave bands was also considered in order to compare with NASA's International Space Station vibratory limit requirements. It should be mentioned that for frequencies above 13 Hz the microgravity mode condition is always accomplished and no warnings appear in any DCMIX3 run.

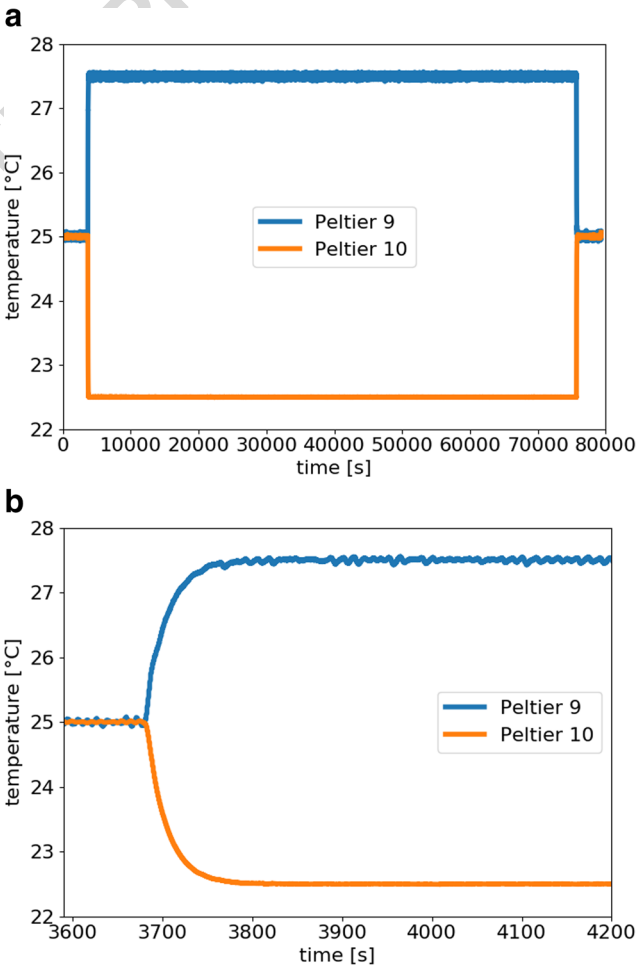

Fig. 10 The temperature profiles for Peltier 9 and 10 during run 04 in cell 4. Top: entire run. Bottom: zoom of the temperature step

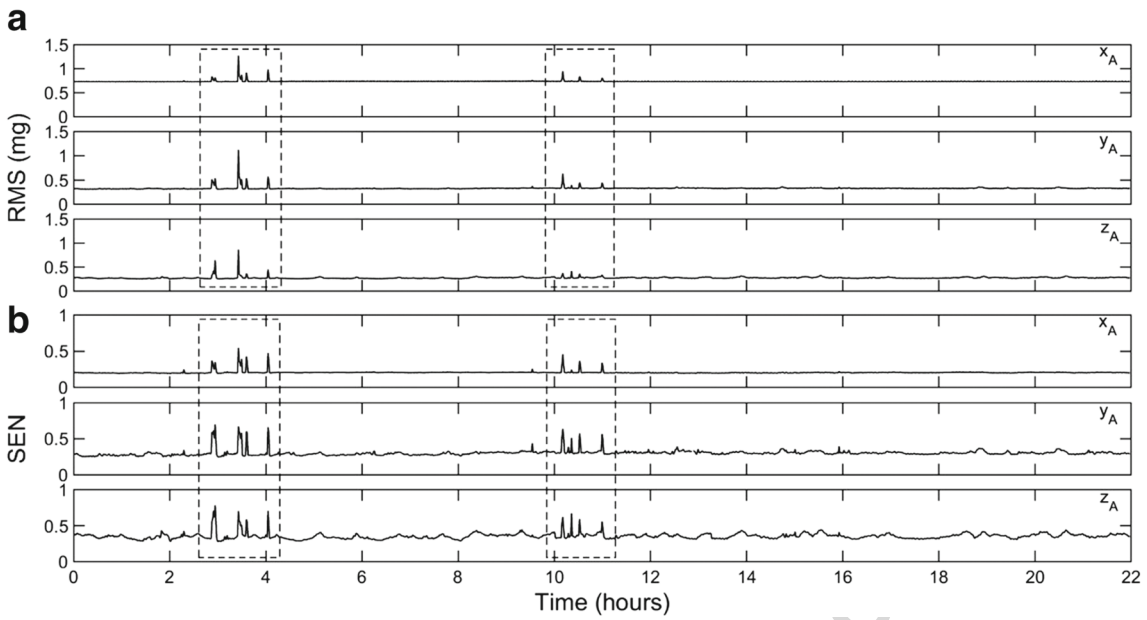

Fig. 11 Minute by minute evolution of RMS (**a**) and SEN (**b**) for the three acceleration components associated to run 23

Other Events

During operations some notable events were logged. The most important one is a shift of the camera position during run 08. Between images taken at 14:46 and 14:49, there is a permanent shift of the visible cell volume by 40 pixels to the left. Since the cell array itself is fixed and the perturbation did not affect the companion cell, the most plausible explanation is a displacement of the movable camera module and, hence, the camera position. Analysis of acceleration data provided by sensors inside MSG confirmed that this shift is correlated with a short but intense low-frequency jitter (Ollé et al. 2017). This jitter, as well as the shift in camera position are deemed non-detrimental for the data quality and analysis. The position shift can be easily accounted for and influences on the diffusion processes are not likely due to the short duration of the jitter.

Other notable events logged during SODI operations refer to incomplete image stacks, which contain less than five images. Also, all stack files were compressed to save disk space and some ZIP files were corrupted (see Table 5). Since a complete run consists of typically 630 stacks, these can be neglected as singular events.

Table 5 A list of all problematic files in the data set

Run	Corrupted files
3	11_0_778C@0027_FR_DSC_160928_201648_0.stk
	11_3_778C@0027_MR_DSC_160928_220323_6.zip
4	11_4_E6A9@0027_MN_DSC_160920_194323_0.zip
5	11_5_E2FD@0027_MN_DSC_160920_002258_6.zip
11	11_0_99D0@0027_FR_DSC_161006_161826_0.zip
15	11_5_05D3@0037_MR_DSC_161004_232405_6.zip
17	11_0_0EA9@0027_FR_DSC_161020_070033_0.stk
	11_2_0EA9@0027_MR_DSC_161020_181713_10.zip
23	11_1_CB9E@0027_MN_DSC_161103_234247_3.zip
24	11_5_A2F0@0004_MN_DSC_161107_080754_10.zip
27	11_0_B287@0025_FR_DSC_161115_075834_0.zip

This includes corrupted ZIP files as well as stacks with less than 5 images

Summary and Conclusions

We have reported on the DCMIX3b campaign aboard the ISS with the aim to measure ternary diffusion, thermodiffusion and Soret coefficients of ternary mixtures composed of water, ethanol and triethylene glycol. After the samples had successfully been delivered to the ISS, the measurements were completed in November 2016, and the data stored on flash disks were made available to the science team in June 2017. First assessments were already made during the measurement campaign. They were based on a small subset of the data that was downlinked in real time and could be refined after the full data set became available.

Besides some minor problems, like a small number of corrupted data files, temperature noise and a shift of the image position caused by an unknown event, two major problems could be identified: the occurrence of a bubble

in cell 3 and laser instabilities during phase stepping. The bubble continued to grow, but it was at least possible to perform one bubble-free measurement with cell 3 at an elevated temperature of 30 °C. In order to have one complete set of measurements for all cells at the same temperature, the nice-to-have runs were used to measure all cells at this elevated temperature. Invalid runs could be avoided almost completely by accurate planning and fast decision-making. Thus, a complete data set at 30 °C and an almost complete data set at 25 °C, containing all cells except cell 3, are now available for further studies.

The laser instabilities have severely perturbed a significant number of runs and in several cases a straightforward data evaluation based on a temporal phase stepping analysis appears not feasible. Nevertheless, we are confident that meaningful information can also be extracted from the affected data sets, and we are currently developing a protocol to extract refractive index gradient information from single images without resorting to temporal phase stepping algorithms.

The information compiled in this document should serve as a starting point for any scientist working on the DCMIX3b data and also help to prepare the forthcoming DCMIX4 experiment as well as planned microgravity experiments on nonequilibrium fluctuations in multicomponent mixtures (Bataller et al. 2016; Baaske et al. 2016). The raw DCMIX3 data (approx. 300 GB compressed) will be available for public access as from June 2018. Researchers interested in the data are kindly asked to contact the corresponding author.

Acknowledgements We want to thank ESA and Roscosmos for providing the flight and operations opportunity and Ana Frutos Pastor and Ewald Kufner from ESA/ESTEC and Ingmar Lafaille and Johan Buytaert from QinetiQ Space for their support during the DCMIX3 campaign. This work has been developed in the framework of the cooperative project DCMIX (No. AO-2009-0858/1056) of the European Space Agency and the Russian Space Agency (Roscosmos)/TsNIIMash. WK and TT acknowledge support from the Deutsches Zentrum für Luft- und Raumfahrt (Grants 50WM1130, 50WM1544). QG, AM, VS and SVV acknowledge support from the PRODEX program of Belgian Federal Science Policy Office (BELSPO). MBA and JOZ acknowledges support from the Spanish 'Agencia Estatal de Investigación' (Grant FIS2014-58950). XR and JG acknowledge support from the Spanish Ministerio de Economia y Competitividad, MINECO (Grant number ESP2014-53603-P). HB and FC acknowledge support from the Centre National d'Etudes Spatiales (Grants 170048/00, 2016/4800000877).

References

Ahadi, A., Ziad Saghir, M.: Eur. Phys. J. E **38**, 25 (2015). https://doi.org/10.1140/epje/i2015-15025-4

Baaske, P., Bataller, H., Braibanti, M., Carpineti, M., Cerbino, R., Croccolo, F., Donev, A., Köhler, W., de Zarate, J.M.O., Vailati, A.: Eur. Phys. J. E **39**, 119 (2016). https://doi.org/10.1140/epje/i2016-16119-1

Bataller, H., Giraudet, C., Croccolo, F., de Zárate, J.M.O.: Microgravity Sci. Tec. **28**, 611 (2016). https://doi.org/10.1007/s12217-016-9517-6

Blanco, P., Bou-Ali, M.M., Platten, J.K., de Mezquia, D.A., Madariaga, J.A., Santamaria, C.: J. Chem. Phys. **132**, 114506 (2010). https://doi.org/10.1063/1.3354114

Bou-Ali, M.M., Ahadi, A., de Mezquia, D.A., Galand, Q., Gebhardt, M., Khlybov, O., Köhler, W., Larranaga, M., Legros, J.C., Lyubimova, T., Mialdun, A., Ryzhkov, I., Saghir, M.Z., Shevtsova, V., Vaerenbergh, S.V.: Eur. Phys. J. E **38**, 30 (2015). https://doi.org/10.1140/epje/i2015-15030-7

Dubert, D., Gavaldà, J., Laverón-Simavilla, A., Ruiz, X., Shevtsova, V.: Acta Astronaut. submitted (2017) Q5

Enge, W., Köhler, W.: Phys. Chem. Chem. Phys. **6**, 2373 (2004). https://doi.org/10.1039/B401087F

Galand, Q., Van Vaerenbergh, S.: Eur. Phys. J. E **38**, 26 (2015). https://doi.org/10.1140/epje/i2015-15026-3

Galliero, G., Bataller, H., Croccolo, F., Vermorel, R., Artola, P.A., Rousseau, B.: Microgravity Sci. Tec. **28**, 79 (2016). https://doi.org/10.1007/s12217-015-9465-6

Gebhardt, M., Köhler, W.: J. Chem. Phys. **142**, 084506 (2015a). https://doi.org/10.1063/1.4908538

Gebhardt, M., Köhler, W.: Eur. Phys. J. E **38**, 24 (2015b). https://doi.org/10.1140/epje/i2015-15024-5

Gebhardt, M., Köhler, W.: J. Chem. Phys. **143**, 164511 (2015c). https://doi.org/10.1063/1.4934718

Gebhardt, M., Köhler, W., Mialdun, A., Yasnou, V., Shevtsova, V.: J. Chem. Phys. **138**, 114503 (2013). https://doi.org/10.1063/1.4795432

Ghiglia, D.C., Pritt, M.D.: Two-Dimensional Phase Unwrapping: Theory Algorithms, and Software. Wiley, New York (1998)

Giglio, M., Vendramini, A.: Phys. Rev. Lett. **34**, 561 (1975). https://doi.org/10.1103/PhysRevLett.34.561

Hariharan, P., Oreb, B.F., Eiju, T.: Appl. Optics **26**, 2504 (1987). https://doi.org/10.1364/AO.26.002504

Haugen, K.B., Firoozabadi, A.: J. Chem. Phys. **122**, 014516 (2005). https://doi.org/10.1063/1.1829033. http://link.aip.org/link/?JCPSA6/122/014516/1

Itoh, K.: Appl. Opt. **21**, 2470 (1982). https://doi.org/10.1364/AO.21.002470

Khlybov, O.A., Ryzhkov, I.I., Lyubimova, T.P.: Eur. Phys. J. E **38**, 29 (2015). https://doi.org/10.1140/epje/i2015-15029-0

Kolodner, P., Williams, H., Moe, C.: J. Chem. Phys. **88**, 6512 (1988)

Königer, A., Meier, B., Köhler, W.: Philos. Mag. **89**, 907 (2009). https://doi.org/10.1080/14786430902814029

Kreis, T.: Handbook of Holographic Interferometry: Optical and Digital Methods. Wiley, New York (2005)

Lapeira, E., Bou-Ali, M.M., Madariaga, J.A., Santamaria, C.: Microgravity Sci. Tec. **28**, 553 (2016). https://doi.org/10.1007/s12217-016-9508-7

Lapeira, E., Gebhardt, M., Triller, T., Mialdun, A., Köhler, W., Shevtsova, V., Bou-Ali, M.M.: J. Chem. Phys. **146**, 094507 (2017). https://doi.org/10.1063/1.4977078

Larrañaga, M., Bou-Ali, M.M., de Mezquia, D.A., Rees, D.A.S., Madariaga, J.A., Santamaria, C., Platten, J.K.: Eur. Phys. J. E **38**, 28 (2015). https://doi.org/10.1140/epje/i2015-15028-1

Leahy-Dios, A., Bou-Ali, M., Platten, J.K., Firoozabadi, A.: J. Chem. Phys. **122**, 234502 (2005). https://doi.org/10.1063/1.1924503

Leaist, D.G., Lu, H.: J. Phys. Chem. **94**, 447 (1990). https://doi.org/10.1021/j100364a077

Legros, J.C., Gaponenko, Y., Mialdun, A., Triller, T., Hammon, A., Bauer, C., Köhler, W., Shevtsova, V.: Phys. Chem. Chem. Phys. **17**, 27713 (2015). https://doi.org/10.1039/C5CP04745E

Lyubimova, T.P., Zubova, N.A.: Microgravity Sci. Tec. **26**, 241 (2014). https://doi.org/10.1007/s12217-014-9383-z

Mazzoni, S., Shevtsova, V., Mialdun, A., Melnikov, D., any, Y.G., Lyubimova, T., Saghir, Z.: Europhysics News **41**, 14 (2010)

Mialdun, A., Legros, J.C., Yasnou, V., Sechenyh, V., Shevtsova, V.: Eur. Phys. J. E **38**, 27 (2015). https://doi.org/10.1140/epje/i2015-15027-2

Ollé, J., Dubert, D., Gavaldà, J., Laveron-Simavilla, A., Ruiz, X., Shevtsova, V.: Acta Astronaut. **140**, 409 (2017). https://doi.org/10.1016/j.actaastro.2017.09.007

Platten, J.K., Bou-Ali, M.M., Costesèque, P., Dutrieux, J.F., Köhler, W., Leppla, C., Wiegand, S., Wittko, G.: Philos. Mag. **83**, 1965 (2003). https://doi.org/10.1080/0141861031000108204

Rapp, B.: Microfluidics: Modeling, Mechanics and Mathematics. Micro and Nano Technologies. Elsevier Science, Amsterdam (2016)

Robinson, D.W., Reid, G.T. (eds.): Interferogram Analysis, Digital Fringe Pattern Measurement Techniques. IOP Publishing Ltd., Bristol and Philadelphia (1993)

Sechenyh, V., Legros, J.C., Shevtsova, V.: J. Chem. Thermodyn. **43**, 1700 (2011). https://doi.org/10.1016/j.jct.2011.05.034

Sechenyh, V., Legros, J.C., Shevtsova, V.: J. Chem. Eng. Data **57**, 1036 (2012). https://doi.org/10.1021/je201277d

Sechenyh, V., Legros, J.C., Shevtsova, V.: J. Chem. Thermodyn. **62**, 64 (2013). https://doi.org/10.1016/j.jct.2013.01.026

Sechenyh, V., Legros, J., Mialdun, A., de Zárate, J.M.O., Shevtsova, V.: J. Phys. Chem. B **120**, 535 (2016). https://doi.org/10.1021/acs.jpcb.5b11143

Servin, M., Quiroga, J.A., Padilla, J.: Fringe Pattern Analysis for Optical Metrology: Theory, Algorithms and Applications. Wiley-VCH, Weinheim (2014)

Shevtsova, V., Sechenyh, V., Nepomnyashchy, A., Legros, J.C.: Philos. Mag. **91**, 3498 (2011). https://doi.org/10.1080/14786435.2011.586376

Shevtsova, V., Santos, C., Sechenyh, V., Legros, J.C., Mialdun, A.: Microgravity Sci. Tec. **25**, 275 (2014a). https://doi.org/10.1007/s12217-013-9349-6

Shevtsova, V., Santos, C., Sechenyh, V., Legros, J.C., Mialdun, A.: Microgravity Sci. Tec. **25**, 275 (2014b). https://doi.org/10.1007/s12217-013-9349-6

Shevtsova, V., Gaponenko, Y.A., Sechenyh, V., Melnikov, D.E., Lyubimova, T., Mialdun, A.: J. Fluid Mech. **767**, 290 (2015). https://doi.org/10.1017/jfm.2015.50

Taylor, R., Krishna, R.: Multicomponent Mass Transfer. Wiley Series in Chemical Engineering. Wiley, New York (1993)

Triller, T., Gebhardt, M., Köhler, W.: Preparation of DCMIX3: characterization of sealing material and physical parameters of samples (internal document)

Q6

AUTHOR QUERIES

AUTHOR PLEASE ANSWER ALL QUERIES:

Q1. Please check all affiliations if captured and presented correctly.
Q2. Please check if captured Keywords are correct.
Q3. Reference citations that appears here were expanded since it only contains URL. Please check if correct and necessary.
Q4. Please provide Article Title for the following references: Ahadi and Ziad Saghir 2015; Baaske et al. 2016; Bataller et al. 2016; Blanco et al. 2010; Bou-Ali et al. 2015; Enge and Köhler 2004; Galand and Van Vaerenbergh 2015; Galliero et al. 2016; Gebhardt and Köhler 2015a, b, c; Gebhardt et al. 2013; Giglio and Vendramini 1975; Haugen and Firoozabadi 2005; Itoh 1982; Khlybov et al. 2015; Kolodner et al. 1988; Königer et al. 2009; Lapeira et al. 2016, 2017; Larrañaga et al. 2015; Leahy-Dios et al. 2005; Leaist et al. 1990; Legros et al. 2015; Lyubimova and Zubova 2014; Mazzoni et al. 2010; Mialdun et al. 2015; Ollé et al. 2017; Platten et al. 2003; Rapp 2016; Sechenyh et al. 2011, 2012, 2013, 2016; Servin et al. 2014; Shevtsova et al. 2011, 2014a, b, 2015.
Q5. Please provide complete bibliographic details for Dubert et al. 2017.
Q6. Please provide complete bibliographic details for Triller et al.